ACS OMEGA

http://pubs.acs.org/journal/acsodf

Article

Nickel Slag/Laterite Soil and Nickel Slag/Iron Sand Nanocomposites: Structural, Optical, and Electromagnetic Absorption Properties

Heryanto Heryanto, Siswanto Siswanto, Roni Rahmat, Abdelmoneim Sulieman, David A. Bradley, and Dahlang Tahir*

Cite This: *ACS Omega* 2023, 8, 18591−18602

Read Online

ACCESS | Metrics & More | Article Recommendations

ABSTRACT: Efforts to produce microwave absorber materials that are inexpensive and environmentally friendly have become a means of greening the environment. The breakthrough can be focused on industrial waste and natural materials for functional purposes and how to enhance their performance. We successfully synthesized nickel slag/laterite soil (NS/LS) and nickel slag/iron sand (NS/IS) nanocomposites using a simple mechanical alloying technique, and the electromagnetic (EM) wave absorption capacities of the nanocomposites were measured using a vector network analyzer. The structural properties of the nanocomposites were analyzed by X-ray diffraction spectroscopy, where the results of the analysis showed that NS/IS has the largest crystallite size (15.69 nm) and the highest EM wave absorption performance. The optical properties of the nanocomposites were determined from their Fourier transform infrared spectra using the Kramers−Kronig relation. As determined through a quantitative analysis of the optical properties, the distance between the longitudinal and transversal optical phonon wavenumber positions ($\Delta(LO - TO) = 65\ cm^{-1}$) is inversely proportional to the reflection loss. The surface morphologies of the nanocomposites were analyzed by scanning electron microscopy, and the particle diameters were observed by binary image and Gaussian distribution analyses. The nanocomposite surface exhibits a graded-like morphology, which indicates multiple reflections of the EM radiation, consequently reducing the EM interference. The best nanocomposite for an attenuated EM wave achieved a reflection loss of −39.14 dB at 5−8 GHz. A low penetration depth has implications for the electrical charge tuning of the storage and composite magnets. Finally, the EM absorption properties of NS/IS and NS/LS indicate a 2-mm-thick environmentally friendly nanocomposite for EM absorption.

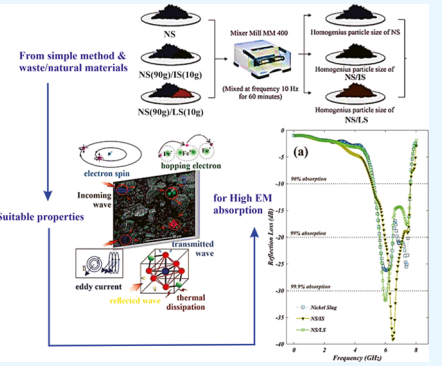

1. INTRODUCTION

Nickel slag (NS) is a waste product from the nickel industry, which can be incorporated with other natural resources to enhance specific characteristics for various applications.[1] The high magnetite content of NS is the primary reason for its use in the absorption of electromagnetic interference (EMI) emissions,[2] sensors,[3] batteries,[4] alkaline activations,[5] and shielding.[6] Fayalite is a perovskite-type material that can be extracted from NS with useful properties, such as ferromagnetism, ferroelectricity, and superconductivity.[7] Fayalite is formed by SiO_2 and has a tetrahedral structure with four O atoms bonding to Si atoms at the center coordinate. Six O atoms surrounding the Fe atoms in tetrahedral SiO_4 can be a suitable combination of metal and semimetal atoms that have the potential to store and absorb energy. Some studies have reported best-performing microwave absorber materials (MAMs), including Fe−Si flakes, Fe−Si−Al alloy powder, $CoFe_2O_4$ pellets, and Fe_3O_4/carbon nanowires, possibly because of their high atomic weight and density.[8−11] Thus, the utilization of fayalite as an electromagnetic (EM) wave absorber could be the focus of further study. Moreover, the low cost and novelty of the utilization of waste materials for MAM applications should be considered. Other studies have used NS as a raw material in the production of Portland cement for road construction[12] or to investigate its effect as a fine aggregate on the properties of concrete containing the same superplasticizer content.[13]

Thin pellets,[14] many layer-structured materials,[15] induced structural defects on surfaces,[16] and surfaces covered by conductive nanosheets[17] are important innovations to change the electrical conductivity and mechanical properties of absorption materials in the military and electronics industries for EMI absorption. Currently, MAM applications have been extended to several fields, such as energy storage[18]/batteries,[4] alkaline activations,[3] sensors,[3] and spacecraft.[19] In Figure 1,

Received: January 20, 2023
Accepted: April 18, 2023
Published: May 18, 2023

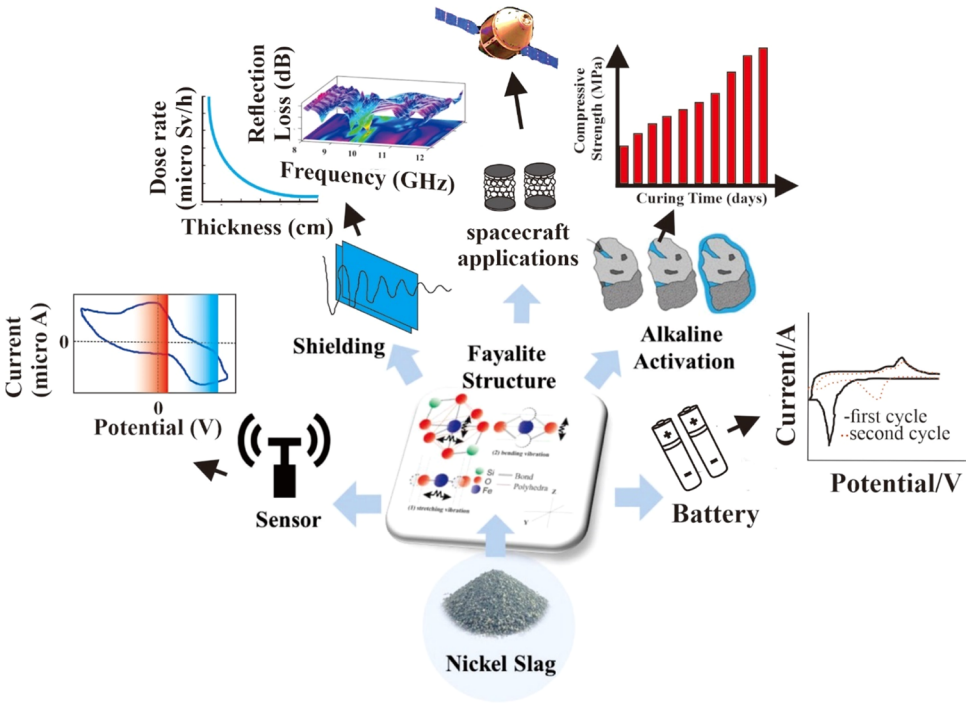

Figure 1. Several applications of fayalite materials.

some applications of fayalite are shown. In advanced application areas, such as batteries, a fayalite nanocomposite (α-Fe_2SiO_4)@C was successfully fabricated via a solid-state reaction under nitrogen gas flow with enormous potential for next-generation lithium-ion batteries. Another study investigated the mineralogical conditions and content of alkali-activated NS glass to adjust the reactivity, mechanical properties, and microstructure of the material. The alkali-activated samples exhibited differences in the chemical composition of their binder gels at an early stage; consequently, the binder became increasingly homogeneous and consisted of a Na−K−Fe−Si gel with Mg, Ca, and Al. Two effective methods of multisensor detection for reinforced concrete structures, namely, active infrared thermography with microwave excitation and eddy current technique, were employed to identify the steel reinforcement features. Although its structure is different from that of fayalite, the 3D hybrid f-Fe_3O_4-VCNTs@rGO hierarchical hybrid formation fabricated by Rajesh Kumar et al. utilized a combination of magnetite and non/semi-magnetite materials to enhance EM interface shielding. An EM interface shield for spacecraft based on self-assembled nanostructures of 3D hierarchical triangles of iron oxide containing vertical carbon nanotubes on reduced graphene oxide hybrids has been fabricated. Thus, various combinations of large and medium atoms can be good absorbers for various fields of physics.

EM wave absorption by electrons and atomic resonance occurs when the interaction energy is dissipated by being converted into heat energy or another energy form.[20] The development of interfacial interactions can regulate the capability of the material to respond to physical phenomena around it. The discovery of the giant electrocaloric effect induced by interfacial charge indicates that multilayered oxide heterostructures hold tremendous promise for the development of highly efficient and scalable solid-state cooling applications.[21,22] A material with a microlayered surface can achieve maximum energy absorption as a multifunctional electronic device. Given that the combination of Fe and Si performs as effectively as a promising MAM, we need to determine how to change the magnetic and electrical properties of NS. Doping methods and their derivatives lead to the formation of defects, which affect the change in electrical conductivity and mechanical properties of the material. Structural defects affect the reflection angle and enhance absorption opportunities, thereby increasing the shielding effectiveness.[23] Impurities derived from natural materials can be used to fine-tune important effects that favor new properties, such as changes in crystallite size, crystal shape, and thermodynamic properties,[24,25] and the selection of materials from nature makes composites an environmentally friendly material during or after use. Therefore, we combine NS with natural materials, such as iron sand (IS) and laterite soil (LS), using the milling method[26,27] to form NS/IS and NS/LS nanocomposites. The performance of IS and LS as construction materials, radioactive waste treatment, environmental remediation, absorbents, and adsorbents exhibits quite favorable capabilities as doping materials.[28−31] Fayalite is a type of mineral with medium electrical conductivity, and we aim to enhance and control its electrical conductivity by doping IS as a material that is dominated by magnetite and LS as a material that is dominated by a combination of Fe and Si, respectively. To the best of our knowledge, only a few reports on environmentally friendly EMI absorbers have been published, and the MAM manufacturing method still takes a long time, uses large amounts of solvents, and is expensive to analyze. Based on these limitations, NS/IS and NS/LS nanocomposites were selected and fabricated by mechanical alloying as an environmentally friendly method. The principle of the mechanical alloying process is that the ball transfers its momentum to the unit mass of the nanocomposite per unit of time as the specific power injected creates a mechanochemical reaction.[32] The mechanochemical process can stabilize

https://doi.org/10.1021/acsomega.3c00423
ACS Omega 2023, 8, 18591−18602

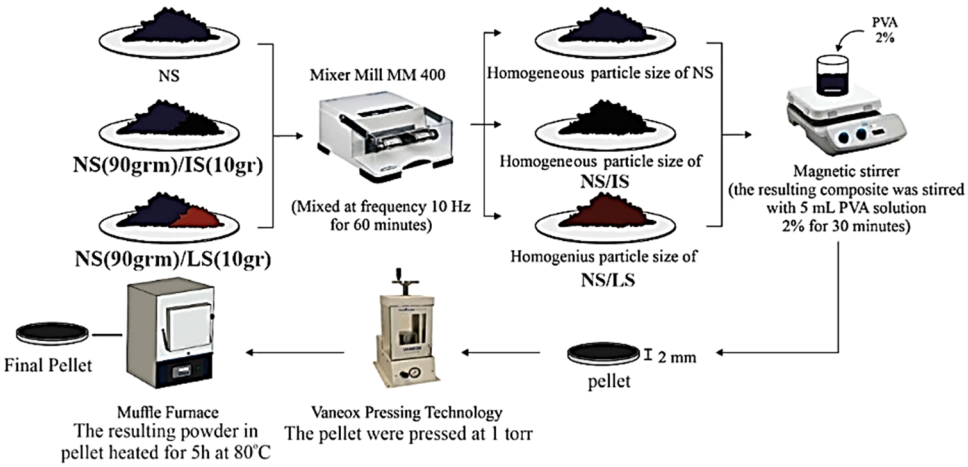

Figure 2. Illustration of pellet compaction for the NS, NS/LS, and NS/IS nanocomposites.

chemical phases, grain repositioning, and crystal defects without using solvents or high temperatures, making it ecosustainable.[33,34]

The chemical composition of this nanocomposite was observed and characterized by X-ray fluorescence (XRF), and its structural properties were analyzed by X-ray diffraction (XRD) spectroscopy. The absorption characteristics were identified by vector network analysis spectroscopy; subsequently, the relationship between reflection loss and structural properties was discussed. The objective of this study was to develop a new, natural, high-performance, and low-cost nanocomposite material based on LS, IS, and NS synthesized via simple and environmentally friendly methods.

2. MATERIAL AND EXPERIMENTAL METHODS

2.1. Materials. NS was collected from the nickel industry of Bantaeng Regency, South Sulawesi, Indonesia. IS was obtained from Pantai Lere, Bima Regency, Nusa Tenggara Barat Province, Indonesia (−8.866147°, 118.527858°), and LS was sourced from the Faculty of Mathematics and Natural Sciences, Hasanuddin University, Indonesia. The compound percentage in all samples was characterized and regulated using an XRF spectrometer. The elemental concentration derived from the XRF results indicated that NS contained 58.12 ± 2% Fe and 19.57 ± 0.8% Si, LS contained 34.25 ± 0.39% Fe and 43.48 ± 0.53% Si, and IS contained 77.29 ± 0.27% Fe and 3.09 ± 0.33% Si.

2.2. Experimental Methods. NS/IS and NS/LS were mixed using a RETSCH Mixer Mill MM 400 at 10 Hz for 1 h to homogenize the particle size of the nanocomposites. For more details, a schematic illustration of the synthesis methods used in this study is shown in Figure 2. The sample abbreviations based on the weights of the nanocomposites are as follows

$$\text{NS} = \text{nickel slag}(90\ \text{g})$$

$$\text{NS/IS} = \text{nickel slag}(90\ \text{g}) + \text{iron sand}(10\ \text{g})$$

$$\text{NS/LS} = \text{nickel slag}(90\ \text{g}) + \text{laterite soil}(10\ \text{g})$$

The optical properties and functional groups of the nanocomposites were analyzed using a Fourier transform infrared (FTIR) spectrophotometer (Shimadzu Corp.) in the wavenumber range of 400−4000 cm^{-1}. The structural properties of the nanocomposites were analyzed via XRD (Shimadzu 7000) using Cu−Kα radiation (λ = 1.54 Å). Scanning electron microscopy (SEM) was used to identify the surface morphology and particle distribution in the nanocomposites. The EM wave absorption properties were measured using a vector network analyzer. The details of the experimental method can be found in our previous publication.[35]

The nanocomposite powder was first mixed with 2% poly(vinyl alcohol) solution and then pelleted by applied pressure of 1 kbar for 10 min until a uniform thickness of 2 mm was reached. The sample pellets were heated for 5 h at 80 °C using a Lab Tech muffle furnace and stored at room temperature for further use.

3. RESULTS AND DISCUSSION

3.1. Fourier Transform Infrared Characterization. Figure 3a shows that the FTIR transmittance spectra were slightly different because of the composition, atomic bond, and physicochemical properties.[36] The functional groups of the nanocomposites were identified as C−OH,[37] C−H,[38] C═O,[39] OH^-,[40] C−O,[41] and Fe−O.[42] In the subsequent analysis, we focused on the wavenumber range of 800−1000 cm^{-1} to identify the stability of the Fe−O bond. These wavenumbers were used to determine the effect of the addition of IS and LS to the NS matrix on the optical properties of the nanocomposite. The strongest absorption bands were attributed to the Fe−O stretching and bending in the octahedral modes, as shown in Figure 3b. The vertical bending vibration occurred because of the connection between one Fe atom and two O atoms moving vertically at different angles. The stretching vibration arises from the longitudinal bending occurring when the Fe atom in the middle of the two O atoms changes like a spring atom, as indicated by the lattice parameters.

The optical properties were determined from the FTIR spectra using the Kramers−Kronig (K−K) relation[43] (Figure 3a).[44] We successfully applied the K−K relation to determine the optical properties from the FTIR spectra of the nanocomposites Fe/CNs/PVA,[45] SPF/starch/chitosan,[46] geopolymer fly ash−metal,[47] and CuO/C.[35] We repeated the methods and the equation for all of the nanocomposites and converted the transmittance spectra into the reflectance spectra $[R(\omega)]$ as follows

$$R(\omega) = 100 - [T(\omega) - A(\omega)] \quad (1)$$

https://doi.org/10.1021/acsomega.3c00423
ACS Omega 2023, 8, 18591−18602

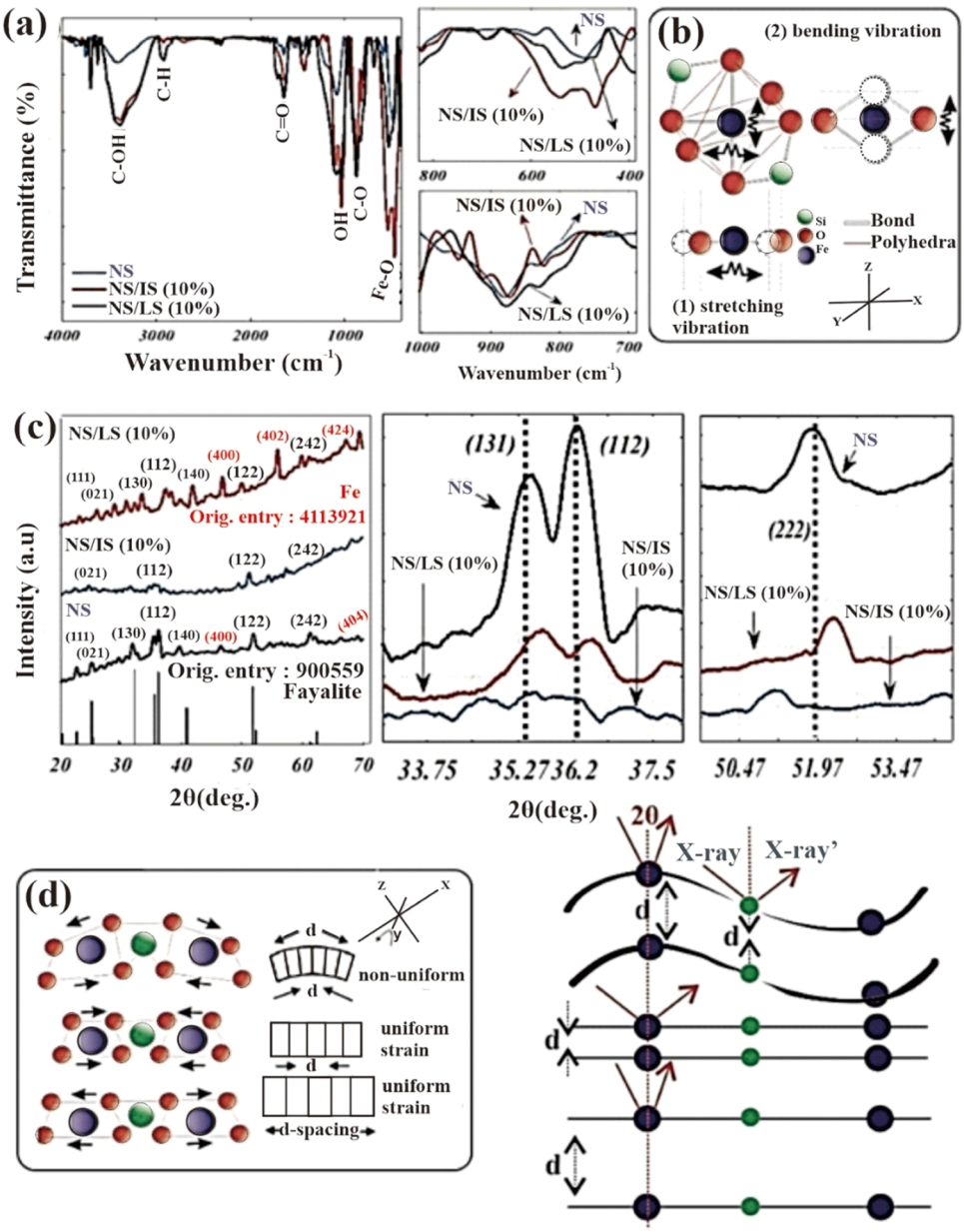

Figure 3. Full Fourier transform infrared (FTIR) spectra: zoomed-in image of the wavenumber range of 700−1000 cm^{-1} (a), schematic illustration of the atomic interaction via stretching and bending vibrations (b), X-ray diffraction (XRD) spectra, including Joint Committee on Powder Diffraction Standard (JCPDS) number 900559 for comparison, and zoomed-in image of the diffraction angles ranging from 33 to 38° and from 50 to 54° (c), and schematic illustrations of the atomic plane based on the *d*-spacing model for uniform NS and nonuniform NS/IS and NS/LS with its effect on the peak of Bragg's angle position (d).

To assess the absorption performance, we applied Lambert's principle[43]

$$A(\omega) = 2 - \log(T(\omega)\%) \tag{2}$$

The optical properties consist of $n(\omega)$ and $k(\omega)$, which can be determined using the following relations[48−51]

$$n(\omega) = \frac{1 - R(\omega)}{1 + R(\omega) - 2\sqrt{R(\omega)}\cos\varphi(\omega)} \tag{3}$$

$$k(\omega) = \frac{2\sqrt{R(\omega)}\sin\varphi(\omega)}{1 + R(\omega) - 2\sqrt{R(\omega)}\cos\varphi(\omega)} \tag{4}$$

where $\varphi(\omega)$ is the phase change between the incident and reflected signals.

$$\varphi(\omega) = -\frac{4\omega_j}{\pi} x\ \Delta\omega\ x \sum_i \frac{\ln(\sqrt{R(\omega)})}{\omega_i^2 - \omega_j^2} \tag{5}$$

Equation 5 was derived from the infrared spectra by applying the K−K relation.[52] The dielectric function is the square of the refractive index and is expressed as follows

$$\hat{\varepsilon}(\omega) = [\tilde{N}(\omega)]^2 = [n(\omega) + ik(\omega)]^2 \tag{6}$$

The real part of the dielectric function is $\varepsilon 1(\omega) = n^2(\omega) - k^2(\omega)$, and the imaginary part of the dielectric function is $\varepsilon_2(\omega) = \varepsilon_2 = 2n(\omega)k(\omega)$. The main peak of $\varepsilon_2(\omega)$ is used to identify the transversal optical phonon denoted by TO and the

https://doi.org/10.1021/acsomega.3c00423
ACS Omega 2023, 8, 18591−18602

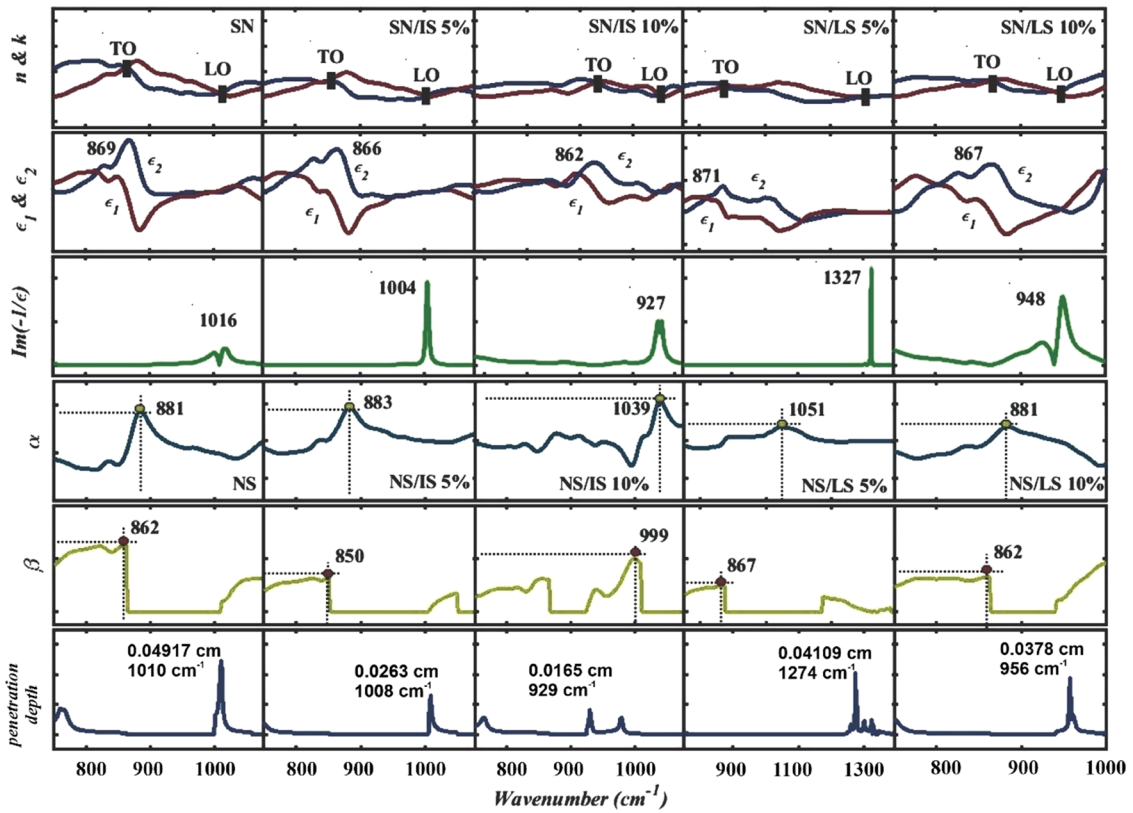

Figure 4. Optical properties (n and k), dielectric functions (ε_1 and ε_2), energy loss function ($Im(-1/\varepsilon)$), attenuation constant (α), phase constant (β), and penetration depth from the quantitative analysis of the FTIR spectra.

longitudinal optical phonon denoted by LO, which is confirmed by the main peak of the energy loss function (ELF) $\left[Im\left(-\frac{1}{\varepsilon_1(\omega)}\right)\right]$

$$Im\left(-\frac{1}{\varepsilon_1(\omega)}\right) = \frac{\varepsilon_1(\omega)}{\varepsilon_1^2(\omega) + \varepsilon_2^2(\omega)} \tag{7}$$

The attenuation constant (α) via ELF, the dielectric function as the input parameter,[53] and the phase constant (β) were determined using the following relations

$$\gamma = \alpha + i\beta \tag{8}$$

$$\alpha = \frac{\sqrt{2}\,\pi}{\lambda_o} \{\varepsilon_2\mu_2 - \varepsilon_1\mu_1 + [(\varepsilon_1\mu_1)^2 + (\varepsilon_2\mu_2)^2 + (\varepsilon_1\mu_2)^2 + (\varepsilon_2\mu_1)^2]^{1/2}\}^{1/2} \tag{9}$$

$$\beta = \frac{\sqrt{2}\,\pi}{\lambda_o} \{\varepsilon_1\mu_1 - \varepsilon_2\mu_2 + [(\varepsilon_2\mu_2)^2 + (\varepsilon_1\mu_1)^2 + (\varepsilon_2\mu_1)^2 + (\varepsilon_2\mu_1)^2]^{1/2}\}^{1/2} \tag{10}$$

The EM radiation can travel inside a material, and its penetration depth was calculated as follows[54]

$$P_d = \frac{\lambda_o}{2\pi} \{\varepsilon_2\mu_2 - \varepsilon_1\mu_1 + [(\varepsilon_1\mu_1)^2 + (\varepsilon_2\mu_2)^2 + (\varepsilon_1\mu_2)^2 + (\varepsilon_2\mu_1)^2]^{1/2}\}^{1/2} \tag{11}$$

The permeability and permittivity of a material are denoted by $\mu_{1,2}$ and $\varepsilon_{1,2}$, respectively. Figure 4 shows the results of the calculation of eq 11.

Figure 4 shows the optical properties (n and k), dielectric functions (ε_1 and ε_2), ELF ($Im(-1/\varepsilon)$), attenuation constant (α), phase constant (β), and penetration depth. The optical properties were used to identify the wavenumber position of the longitudinal (LO) and transversal (TO) optical phonon vibration modes. We have successfully identified the LO and TO to analyze the optical properties of nanocomposites.[55] The peaks of ε_2 and $Im(-1/\varepsilon)$ are similar to the TO and LO positions, respectively. The quantitative analysis of the FTIR spectra shows that $\Delta(\mathrm{LO} - \mathrm{TO})$ for NS is wider than for NS/LS and NS/IS nanocomposites. The wider $\Delta(\mathrm{LO} - \mathrm{TO})$ indicates the stable bonding of the nanocomposite,[56] and the higher value of NS indicates that the bonding is more stable than others. This finding can be attributed to the differences in bond stability because of the effects of doping and the formation of new bonds; thus, the addition of IS and LS successfully reconditions the initial state of the fayalite structure in NS and can stimulate coherent vibrations.[57]

In Figure 4 (fourth row), the NS/IS nanocomposite exhibits the highest wavenumber position change of α, which can be attributed to the structural properties and more compact bonds.[58−60] Furthermore, the highest wavenumber position for the attenuation and phase constants of NS/IS corresponds to the amount of magnetite and the atomic density of IS.[61,62] In

https://doi.org/10.1021/acsomega.3c00423
ACS Omega 2023, 8, 18591−18602

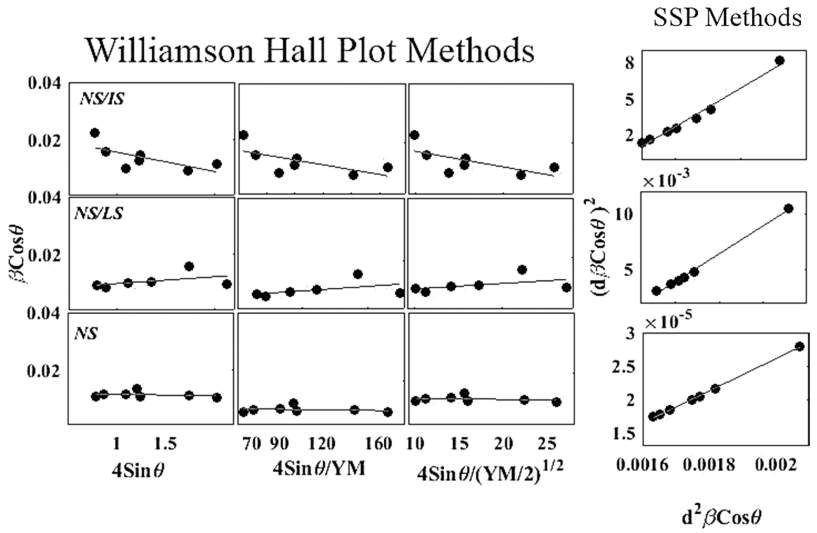

Figure 5. Quantitative analysis of the XRD patterns of the nanocomposites using the Williamson−Hall and size−strain plot methods.

Table 1. *d*-Spacing, Lattice Parameters, and Linear Line Equation Fitting from Figure 5

ID	*d*-spacing	lattice parameters (Å)	volume (Å^3)	$y = ax + b$	UDM	USDM	UDEDM	SSP
NS	2.648	a: 4.78 ± 4 × 10^{-3}		slope	−0.00042	−5.17 × 10^{-6}	−3.31 × 10^{-5}	0.024164
		b: 10.31 ± 8 × 10^{-3}	298.3 ± 0.678	int.	0.012059	0.012059	0.01205	−2.22 × 10^{-5}
		c: 6.04 ± 0.004						
		b: 10.26 ± 0.006	292.6 ± 0.441	int.	0.007611	0.0076	0.00761	−0.00614
		c: 5.97 ± 0.003						
NS/IS	2.661	a: 6.23 ± 0.18		slope	−0.00665	−8.11 × 10^{-5}	5.20 × 10^{-4}	0.031955
		b: 9.54 ± 0.107	337.1 ± 17.32	int.	0.022354	2.24 × 10^{-2}	0.02235	−3.7 × 10^{-5}
		c: 5.66 ± 6.4 × 10^{-2}						

general, the higher the attenuation coefficient, the less the EM energy transmitted, which means that the density of the nanocomposite increases. For β in Figure 4 (fifth row), NS/LS shows the minimum peak and consistent wavenumber position with NS. This is comparable to a transmission line, where low-intensity β indicates an increase in phase velocity. Some small peaks of α and β are detected, which can be attributed to the contribution of the purity level and the large and nonuniform shape of the particles in the nanocomposites.[63] Given these factors, the nanocomposites exhibit different wavelengths in the frequency domain.

In terms of infrared penetration depth into nanocomposites shown in Figure 4 (last row), NS/IS nanocomposites have lower yields than NS/LS and NS nanocomposites. The difference in the penetration depth of EM waves in nanocomposites can be attributed to the atomic arrangement that can be related to the conversion of energy into atomic structural vibration.[64] It is also possibly due to the dominant Fe in the interaction processes.[65] However, NS samples and NS/LS nanocomposites require high penetration depth to absorb EM, resulting in low performance as MAM.

3.2. X-ray Diffraction. The XRD spectra of NS, NS/LS, and NS/IS are shown in Figure 3c, with the corresponding JCPDS number 900559 to identify the crystal plane. The diffraction peaks in reported ref 66 indicated that the fayalite (Fe_2SiO_4) phase was dominant in the NS sample. Fayalite is an orthorhombic structure with the (111), (021), (130), (112), (140), (222), and (242) crystal planes corresponding to the diffraction peaks at 22.37, 24.89, 31.68, 36.2, 40.41, 51.97, and 62.04°, respectively. Another phase detected was Fe, with JCPDS number 4113921, with the (400), (402), (424), and (404) crystal planes at 2θ angles of 45.15, 53.5, 67.54, and 68.36°, respectively. The multiple phases may have originated from the matrix material used, and the basic material in this study is waste. The diffraction peaks of NS/LS and NS/IS shifted to a higher wavelength for LS and a lower wavelength for IS from the pure NS, as indicated by the diffraction shift from 33 to 38° and from 50 to 54° shown in Figure 3c. The (222) crystal plane of NS/LS exhibited a shrinkage strain and that of NS/IS showed a widening strain. The broadening peaks indicated the change in the crystallite size, as reported in ref 67, and the convolution between crystallite size and micro-strain can be calculated using the Scherrer, Williamson−Hall (W−H), and size−strain plot (SSP) methods. The crystallite size was calculated using the Scherrer method by focusing on the diffraction peaks of the fayalite phase using $D_s = k\lambda_{Cu}/\beta \cos\theta$,[68] where the crystallite size determined using the Scherrer method is (D_s), the full width at half-maximum is (β), where $\beta^2 = \beta^2_{measures} - \beta^2_{instrumental}$, the Scherrer constant or shape factor (k) is equal to 1 for orthorhombic structures, the wavelength ($\lambda_{Cu} - k\alpha$) is equal to 1.5418 Å, and θ is Bragg's angle. In ref 69, the calculated crystallite size can also be included, and the stacking fault of the nanocomposite can also be predicted using the W−H method. The aforementioned method has been successfully used to obtain our previously reported results for CuO/C,[35] Fe_3O_4/C,[67] and $Ca_2Fe_2O_5$−AC/chitosan.[70] In determining the structural parameters using XRD, if the diffraction peaks of the nanocomposites are assumed to be isotropic, then the SSP method can be applied to calculate the size−strain parameters. In this method, the

https://doi.org/10.1021/acsomega.3c00423
ACS Omega 2023, 8, 18591−18602

strain profile is denoted by a Gaussian function and the crystallite size is denoted by a Lorentzian function.[71,72] Figure 5 shows W−H and SSP methods for determining the slope and intercept based on the contribution of microstrains to the isotropic diffraction spectra.

Table 1 shows the *d*-spacing, lattice parameters, and linear line equation fitting obtained from the slope orientation affected by the *d*-spacing and Young's modulus of the crystal, as indicated by peak broadening. The highest dislocation was observed for NS/IS because of the infiltration of Fe atoms, which have a large atomic radius, and the intrinsic strain in fayalite. In Figure 5, the positive and negative slopes that resulted from plotting using the W−H method are related to the lattice rearrangement and lattice shrinkage, respectively.[73] As shown in Figure 3d, lattice strain needs to be observed as it is caused by the increase and decrease in the *d*-spacing having a linear effect on the early and late 2θ positions. In a related study, the strain mechanism for the elastic properties of the material was linked to the energy density of the unit cell.[74] The change in lattice size will also provide opportunities for outer atoms to fill, substitute, or sit in suitable positions, thus triggering changes in the magnetic saturation and coercivity properties of the material.[75] The quantitative analysis of the XRD spectra using the W−H and SSP methods is shown in Table 2.

Table 2. Structural Properties Determined from the Quantitative Analysis of the X-ray Diffraction Spectra of the Nanocomposites

Scherrer	(*hkl*)	NS	NS/LS	NS/IS
Ds	(021)	14.05	16.05	6.69
	(111)	13.08	17.64	9.45
	(130)	12.76	14.94	15.00
	(131)	11.20	14.89	11.97
	(112)	13.80	14.16	10.35
	(222)	13.28	9.53	16.24
	(242)	14.21	15.43	12.77
ε_s	(021)	0.0137	0.0119	0.0292
	(111)	0.0132	0.0097	0.0181
	(130)	0.0108	0.0092	0.0093
	(131)	0.0111	0.0093	0.0103
	(112)	0.0088	0.0079	0.0118
	(222)	0.0065	0.0091	0.0054
	(242)	0.0052	0.0046	0.0058
Williamson−Hall	parameters	NS	NS/LS	NS/IS
UDM	D_{WH}	12.53	19.85	6.77
	ε	0.42	0.234	0.66
USDM	D_{WH}	12.51	19.87	6.75
	ε	0.5	0.25	0.72
UDEDM	D_{WH}	12.56	19.80	6.77
	ε	0.44	0.435	0.69
SSP	D_{WH}	10.93	10.43	8.33
	$\varepsilon \times 10^{-2}$	47.21	78.30	60.91

The average crystallite size of the NS/IS nanocomposite is the largest at 15.69 nm, whereas that of the NS/LS nanocomposite is the smallest at 10.09 nm and that of NS is 12.81 nm, which depends on the atomic dislocation by the Burgers and line vectors. The influence of the crystallite size in enhancing the EM wave absorption properties by surface modification was reported in ref 76.

3.3. Scanning Electron Microscopy. Figure 6 shows the SEM images of different shapes and diameters of particles. The second column in Figure 6 shows the enlarged image on the left side, and we have included a binary image for a clear particle boundary observation. The grain boundary diameter of the particle was observed at the particle edge and used to calculate the distribution of the average particle diameter. The average particle diameter, as shown in the third column in Figure 6, of NS/LS is (3.5 ± 1.5) μm, that of NS/IS is (11.2 ± 3) μm, and that of NS is (13.5 ± 6.5) μm.

The nanocomposite surface exhibits a graded-like morphology, which indicates multiple reflections of the EM radiation, consequently reducing the EMI. The effect of multiple scattering supported EMI reduction and the conversion of the incoming energy into a different form of energy or heat. The heat affected the lattice, phonon, and plasmon vibration, as well as the magnetic domain wall and electron spin loss, as described in refs 77−79.

3.4. Vector Network Analysis. Figure 7 shows the reflection loss in the maximum frequency range of 1−8 GHz measured using a vector network analyzer. The efficiency of absorbing EM waves can be identified by the broad bandwidth and lowest reflection loss.

In Figure 7 and Table 3, the effectiveness of the nanocomposites in absorbing the EM wave is indicated by the broadest bandwidth and lowest reflection loss of NS/LS, followed by NS/IS and NS. The relationship between the structural and optical properties and the EM wave absorption performance is shown in Table 3.

Table 3 shows that LS and IS successfully modified the structural and optical properties of NS along with its morphology and internal reflection, consequently enhancing the EMI absorption.[80−82] Energy dissipation was reduced probably because of the reorientated magnetic domain, indicated by the magnetic particles present at the nanocomposite surface.[83−85] Several physical phenomena can be correlated to the released energy from the incoming wave to the nanocomposite, such as thermal energy, the generation of new magnetic moment, electron spin loss, hooping of electrons, and eddy current loss.[86−88] We also believe in reporting the EM absorption phenomena affected by the step ladder shape of the nanocomposite surface, which directly decreased the EMI wave during multiple interactions to form multiple reflections.[89]

The dielectric constant (ε) indicates how much a material can store electrical charge, and the magnetic permeability (μ) relates to how easily a material is magnetized.[90,91] The penetration depth is the depth that EM energy can penetrate before being absorbed or attenuated.[95] Impedance matching also plays an important role in determining how the electric and magnetic fields can propagate through the material, which indicates the effectiveness of the nanocomposites in absorbing EM energy.[92] The penetration depth of the material should be proportional to the thickness of the material to ensure effective EM absorption. In general, materials with greater dielectric constant and magnetic permeability have a thinner penetration depth and thus are more effective as a shield; for more details, the correlation results are shown in Figure 4 (last row) and Figure 7 (middle panel). The relationship between these properties is essential to achieve a balance between penetration depth and impedance.

The capability of the material to respond to a magnetic field also plays a prominent role in the absorption of EMI. The

https://doi.org/10.1021/acsomega.3c00423
ACS Omega 2023, 8, 18591−18602

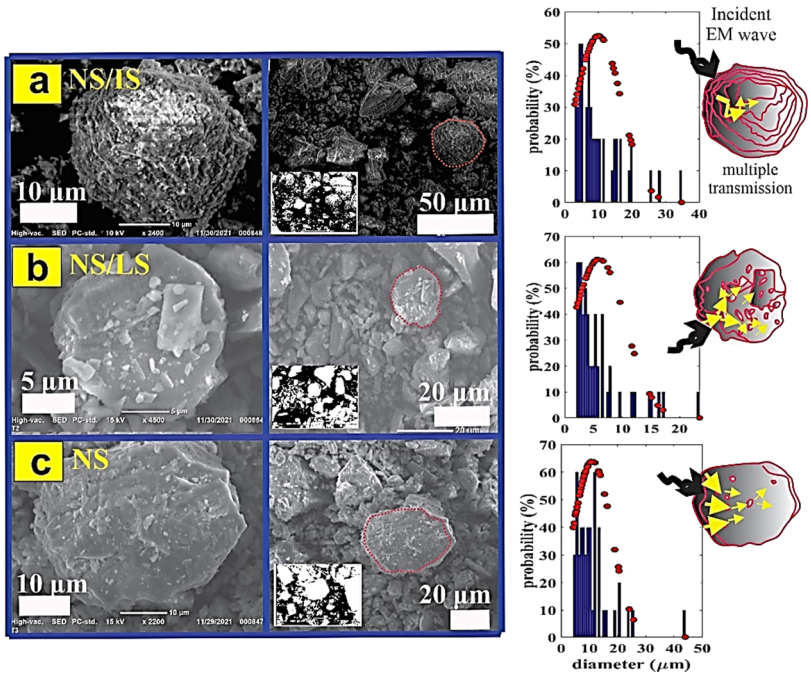

Figure 6. Scanning electron microscopy images of the nanocomposite (left) (a) for sample NS/IS, (b) for NS/LS, and (c) for NS, binary image (center) for the size 20 μm and corresponding probability of particle size prediction from the middle rows (right).

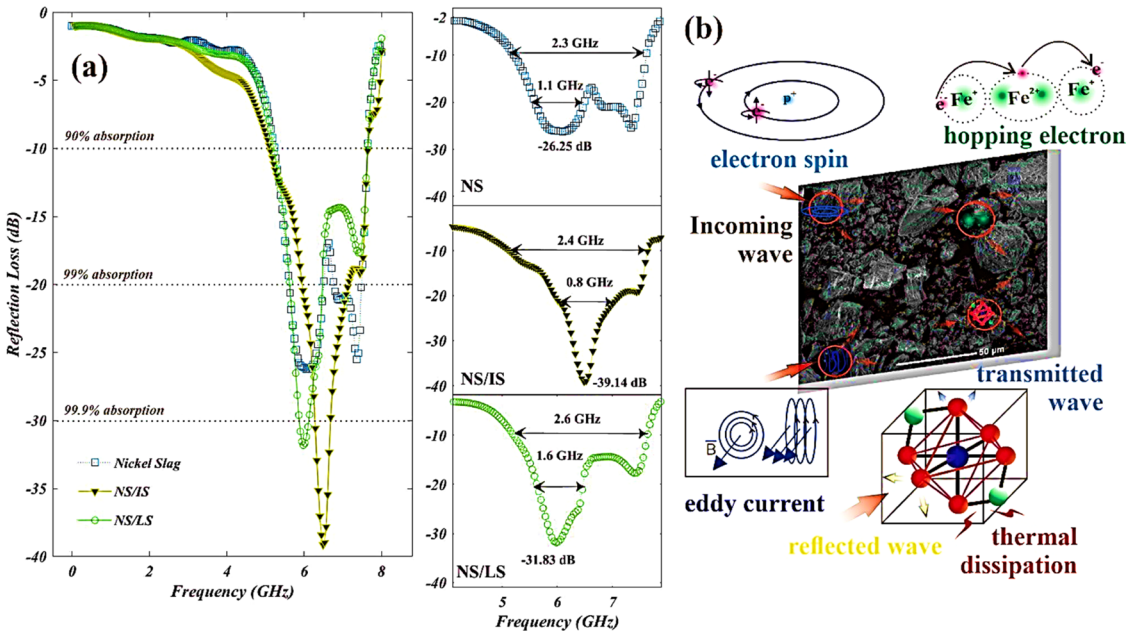

Figure 7. Reflection loss of nanocomposites in the frequency range of 0−8 GHz (a) and several illustrations of a physical phenomenon that describes the interaction of electromagnetic wave attenuation when interacting with nanocomposites (b).

appropriate permeability properties can work optimally at certain working frequencies so that the magnetization process will occur to dissipate the EM energy. For the range of 1−10 GHz, only a few studies reported the corresponding permeability related to this study.[93−95] The effective permeability for frequencies 5 ≥ 7 ≤ 10 GHz is determined to be 2.4 ≥ 2.6 ≤ 2.9. In addition to the permeability properties, the conductive properties of materials also affect the performance of MAMs. The conductive properties of materials contribute to the conversion of microwave energy into heat through resistive losses; meanwhile, the high dielectric constant enables the storage of EM energy, which can increase absorption. Overall, structural and optical properties, interfacial interaction, and magnetic, conductive, and dielectric properties, as well as specific frequencies and polarization, are the main factors that influence the absorption of incident EM radiation.

Future perspectives and possible challenges for metal-based and semimetal-based materials used in the field of EM absorption and how they can be applied are discussed by comparing their properties and preparation methods. In ref 96, excellent absorption performance was observed from Co/

https://doi.org/10.1021/acsomega.3c00423
ACS Omega 2023, 8, 18591−18602

Table 3. Average Crystallite Size, Penetration Depth, Particle Diameter, Distance between LO and TO Phonon Vibration, and Bandwidth of the Reflection Loss

			diameter		reflection loss		
samples	average crystallite size (nm)	penetration depth (cm)	particle size (μm)	Δ(LO − TO) (cm^{-1})	frequency (GHz)	bandwidth (cm^{-1})	dB
NS	12.81	0.049	13.5 ± 6.5	147	10	2.3	−26.25
					20	1.1	
NS/LS	10.09	0.037	3.5 ± 1.5	81	10	2.6	−31.83
					20	1.6	
NS/IS	15.69	0.016	11.2 ± 3.1	65	10	2.4	−39.14
					20	0.8	

Fe_2O_3 with a unique atomic arrangement obtained from a <20% carbon doping system using the mechanical alloying method. Alternatively, nonideal crystal conditions contribute to the EM absorption capability of the material. In ref 97, the polycrystalline oxide was prepared via a low-cost microemulsion method. As the concentration of yttrium ions increased, their electrical and magnetic properties changed. This variation also affected the magnetic behavior of the prepared Mn-based spinel ferrites, which is responsible for increasing the magnetic moment and saturation magnetization (M_s). The secondary phase also affected the grain boundaries by increasing the Y^{3+}−O^{2-} bond energy that decreased the grain size, which is responsible for the increase in the H_c value. Nanomaterials also have an advanced role to play in EM absorption. Particles smaller than 100 nm and possessing unique optical and electrical properties due to their small size are designed to have a high surface area-to-volume ratio, which ensures their effectiveness in absorbing EM radiation. Thus, nanomaterials can be engineered to have specific shapes and sizes, which enable precise control over their optical and electrical properties, such as carbon-based nanomaterials/allotropes[98] and 1D−2D sp^2 carbon nanomaterials.[99] Based on the properties of the material, EM-absorbing devices can be designed to have specific control of the absorption properties. These materials can also be lightweight and flexible, making antenna devices easier to incorporate.

4. CONCLUSIONS

The mechanical alloying method has been successfully used to fabricate nanocomposites using materials from NS with natural materials, such as IS and LS. The NS/LS nanocomposite exhibited the best bandwidth EMI absorption that has a good correlation to the smaller particle size, which resulted in the formation of multiple reflections. By contrast, the NS/IS nanocomposite showed the largest attenuation of EM wave energy, which can be attributed to the shortening optical wavenumber position for Δ(LO − TO) phonon vibrations, where it can stimulate the presence of coherent vibrations.

■ ASSOCIATED CONTENT

Data Availability Statement

All data and materials generated or analyzed during this study were included in this article.

■ AUTHOR INFORMATION

Corresponding Author

Dahlang Tahir − *Department of Physics, Hasanuddin University, Makassar 90245, Indonesia;* orcid.org/0000-0002-8241-3604; Phone: (+62) 411-587634; Email: dtahir@fmipa.unhas.ac.id

Authors

Heryanto Heryanto − *Department of Physics, Hasanuddin University, Makassar 90245, Indonesia*

Siswanto Siswanto − *Department of Statistics, Hasanuddin University, Makassar 90245, Indonesia*

Roni Rahmat − *Department of Physics, Hasanuddin University, Makassar 90245, Indonesia*

Abdelmoneim Sulieman − *Department of Radiology and Medical Imaging Sciences, College of Applied Medical Sciences, Prince Sattam bin Abdulaziz University, Alkharj 11942, Saudi Arabia*

David A. Bradley − *Centre for Nuclear and Radiation Physics, Department of Physics, University of Surrey, Guildford GU2 7XH, United Kingdom; Centre for Applied Physics and Radiation Technologies, School of Engineering and Technology, Sunway University, 47500 Bandar Sunway, Selangor, Malaysia*

Complete contact information is available at: https://pubs.acs.org/10.1021/acsomega.3c00423

Author Contributions

H.H.: writing, illustration, and editing—original draft. S.S. and R.R.: software, validation writing—original draft. A.S., D.A.B., and D.T.: writing—original draft, editing, review, and finalization.

Notes

The authors declare no competing financial interest.

■ ACKNOWLEDGMENTS

This work was supported by PDPU (Penelitian Dosen Pemula): 1477/UN4.22/PT.01.03/2022 and funded by Hasanuddin University, Indonesia.

■ REFERENCES

(1) Dang, D. T.; Nguyen, M. T.; Nguyen, T. P.; Isawa, T.; Ta, Y.; Sato, R. Mechanical Properties of Steel Slag Replaced Mineral Aggregate for Road Base/Sub-Base Application Based Vietnam and Japan Standard. *Environ. Sci. Pollut. Res.* **2022**, *29*, 42067−42073.

(2) Yan, P.; Shen, Y.; Du, X.; Chong, J. Microwave Absorption Properties of Magnetite Particles Extracted from Nickel Slag. *Materials* **2020**, *13*, No. 2162.

(3) Wibowo, D.; Sufandy, Y.; Irwan, I.; Azis, T.; Maulidiyah, M.; Nurdin, M. Investigation of Nickel Slag Waste as a Modifier on Graphene-TiO2 Microstructure for Sensing Phenolic Compound. *J. Mater. Sci.: Mater. Electron.* **2020**, *31*, 14375−14383.

(4) Zhang, Q.; Ge, S.; Xue, H.; Wang, X.; Sun, H.; Li, A. Fabrication of a Fayalite@C Nanocomposite with Superior Lithium Storage for Lithium Ion Battery Anodes. *RSC Adv.* **2014**, *4*, 58260−58264.

(5) Adediran, A.; Yliniemi, J.; Illikainen, M. Mineralogy and Glass Content of Fe-rich Fayalite Slag Size Fractions and Their Effect on

https://doi.org/10.1021/acsomega.3c00423
ACS Omega 2023, 8, 18591−18602

Alkali Activation and Leaching of Heavy Metals. *Int. J. Ceram. Eng. Sci.* **2021**, *3*, 287−300.
(6) Fan, Y.; Zhang, B.; Song, J.; Volski, V.; Vandenbosch, G. A. E.; Guo, M. An Innovated Application of Reutilize Copper Smelter Slag for Cement-Based Electromagnetic Interference Composites. *Sci. Rep.* **2018**, *8*, No. 16155.
(7) Zhao, J.; Gao, J.; Li, W.; Qian, Y.; Shen, X.; Wang, X.; Shen, X.; Hu, Z.; Dong, C.; Huang, Q.; Cao, L.; Li, Z.; Zhang, J.; Ren, C.; Duan, L.; Liu, Q.; Yu, R.; Ren, Y.; Weng, S.-C.; Lin, H.-J.; Chen, C.-T.; Tjeng, L.-H.; Long, Y.; Deng, Z.; Zhu, J.; Wang, X.; Weng, H.; Yu, R.; Greenblatt, M.; Jin, C. A Combinatory Ferroelectric Compound Bridging Simple ABO3 and A-Site-Ordered Quadruple Perovskite. *Nat. Commun.* **2021**, *12*, No. 747.
(8) Gong, Y. X.; Zhen, L.; Jiang, J. T.; Xu, C. Y.; Shao, W. Z. Preparation of CoFe Alloy Nanoparticles with Tunable Electromagnetic Wave Absorption Performance. *J. Magn. Magn. Mater.* **2009**, *321*, 3702−3705.
(9) Hou, C.-l.; Li, T.; Zhao, T.; Liu, H.; Liu, L.; Zhang, W. Electromagnetic Wave Absorbing Properties of Multi-Wall Carbon Nanotube/Fe3O4 Hybrid Materials. *New Carbon Mater.* **2013**, *28*, 184−190.
(10) Tian, N.; You, C. Y.; Liu, J.; Qu, F.; Wang, C. H.; Lu, Z. X. Electromagnetic Microwave Absorption of Fe−Si Flakes with Different Mixtures. *J. Magn. Magn. Mater.* **2013**, *339*, 114−118.
(11) Lee, K. S.; Yun, Y. C.; Jeong, I. B.; Kim, S. S. Microwave Absorbing Properties of Flaky Fe-Si-Al Alloy Powder-Rubber Composites. *Mater. Sci. Forum* **2007**, *534*−*536*, 1465−1468.
(12) Wu, Q.; Wu, Y.; Tong, W.; Ma, H. Utilization of Nickel Slag as Raw Material in the Production of Portland Cement for Road Construction. *Constr. Build Mater.* **2018**, *193*, 426−434.
(13) Sun, J.; Feng, J.; Chen, Z. Effect of Ferronickel Slag as Fine Aggregate on Properties of Concrete. *Constr. Build Mater.* **2019**, *206*, 201−209.
(14) Gao, S.; Chen, L.; Zhang, Y.; Shan, J. Fe Nanoparticles Decorated in Residual Carbon from Coal Gasification Fine Slag as an Ultra-Thin Wideband Microwave Absorber. *Compos. Sci. Technol.* **2021**, *213*, No. 108921.
(15) Kumar, R.; Sahoo, S.; Joanni, E.; Singh, R. K.; Tan, W. K.; Kar, K. K.; Matsuda, A. Recent Progress on Carbon-Based Composite Materials for Microwave Electromagnetic Interference Shielding. *Carbon* **2021**, *177*, 304−331.
(16) Kumar, R.; Singh, R. K.; Tiwari, V. S.; Yadav, A.; Savu, R.; Vaz, A. R.; Moshkalev, S. A. Enhanced Magnetic Performance of Iron Oxide Nanoparticles Anchored Pristine/ N-Doped Multi-Walled Carbon Nanotubes by Microwave-Assisted Approach. *J. Alloys Compd.* **2017**, *695*, 1793−1801.
(17) Kumar, R.; Macedo, W. C.; Singh, R. K.; Tiwari, V. S.; Constantino, C. J. L.; Matsuda, A.; Moshkalev, S. A. Nitrogen−Sulfur Co-Doped Reduced Graphene Oxide-Nickel Oxide Nanoparticle Composites for Electromagnetic Interference Shielding. *ACS Appl. Nano Mater.* **2019**, *2*, 4626−4636.
(18) Kumar, R.; Sahoo, S.; Joanni, E.; Singh, R. K.; Kar, K. K. Microwave as a Tool for Synthesis of Carbon-Based Electrodes for Energy Storage. *ACS Appl. Mater. Interfaces* **2022**, *14*, 20306−20325.
(19) Kumar, R.; Alaferdov, A. V.; Singh, R. K.; Singh, A. K.; Shah, J.; Kotnala, R. K.; Singh, K.; Suda, Y.; Moshkalev, S. A. Self-Assembled Nanostructures of 3D Hierarchical Faceted-Iron Oxide Containing Vertical Carbon Nanotubes on Reduced Graphene Oxide Hybrids for Enhanced Electromagnetic Interface Shielding. *Composites, Part B* **2019**, *168*, 66−76.
(20) Guo, Y.; Zhang, X.; Feng, X.; Jian, X.; Zhang, L.; Deng, L. Non-Isothermal Oxidation Kinetics of FeSiAl Alloy Powder for Microwave Absorption at High Temperature. *Composites, Part B* **2018**, *155*, 282−287.
(21) Wang, Z.; Dai, L.; Yao, J.; Guo, T.; Hrynsphan, D.; Tatsiana, S.; Chen, J. Improvement of Alcaligenes Sp.TB Performance by Fe-Pd/Multi-Walled Carbon Nanotubes: Enriched Denitrification Pathways and Accelerated Electron Transport. *Bioresour. Technol.* **2021**, *327*, No. 124785.
(22) Shirsath, S. E.; Assadi, M. H. N.; Zhang, J.; Kumar, N.; Gaikwad, A. S.; Yang, J.; Maynard-Casely, H. E.; Tay, Y. Y.; Du, J.; Wang, H.; Yao, Y.; Chen, Z.; Zhang, J.; Zhang, S.; Li, S.; Wang, D. Interface-Driven Multiferroicity in Cubic BaTiO3-SrTiO3 Nanocomposites. *ACS Nano* **2022**, *16*, 15413−15424.
(23) Kumar, R.; Sahoo, S.; Joanni, E.; Singh, R. K.; Tan, W. K.; Moshkalev, S. A.; Matsuda, A.; Kar, K. K. Heteroatom Doping of 2D Graphene Materials for Electromagnetic Interference Shielding: A Review of Recent Progress. *Crit. Rev. Solid State Mater. Sci.* **2022**, *47*, 570−619.
(24) Duan, J.; Farrugia, D.; Davis, C.; Li, Z. Effect of Impurities on the Microstructure and Mechanical Properties of a Low Carbon Steel. *Ironmaking Steelmaking* **2022**, *49*, 140−146.
(25) Abdi-Jalebi, M.; Ibrahim Dar, M.; Sadhanala, A.; Johansson, E. M. J.; Pazoki, M. Chapter 3 - Optical Absorption and Photoluminescence Spectroscopy. In *Characterization Techniques for Perovskite Solar Cell Materials*; Pazoki, M.; Hagfeldt, A.; Edvinsson, T., Eds.; Elsevier, 2020; pp 49−79 DOI: 10.1016/B978-0-12-814727-6.00003-7.
(26) Rashidi, N. A.; Yusup, S. A Review on Recent Technological Advancement in the Activated Carbon Production from Oil Palm Wastes. *Chem. Eng. J.* **2017**, *314*, 277−290.
(27) Menya, E.; Olupot, P. W.; Storz, H.; Lubwama, M.; Kiros, Y. Production and Performance of Activated Carbon from Rice Husks for Removal of Natural Organic Matter from Water: A Review. *Chem. Eng. Res. Des.* **2018**, *129*, 271−296.
(28) Li, J.; Ye, W.; Chen, C. Chapter 5 - Removal of Toxic/Radioactive Metal Ions by Metal-Organic Framework-Based Materials. In *Interface Science and Technology*; Chen, C., Ed.; Elsevier, 2019; Vol. *29*, pp 217−279 DOI: 10.1016/B978-0-08-102727-1.00005-4.
(29) Egenti, C.; Khatib, J. M. 13 - Sustainability of Compressed Earth as a Construction Material. In *Sustainability of Construction Materials*, 2nd ed.; Khatib, J. M., Ed.; Woodhead Publishing, 2016; pp 309−341 DOI: 10.1016/B978-0-08-100370-1.00013-5.
(30) Amjlef, A.; Khrach, S.; Ait El Fakir, A.; Farsad, S.; Et-Taleb, S.; el Alem, N. Adsorptive Properties Investigation of Natural Sand as Adsorbent for Methylene Blue Removal from Contaminated Water. *Nanotechnol. Environ. Eng.* **2021**, *6*, 26.
(31) Handoko, E.; Sugihartono, I.; Marpaung, M. A.; Budi, S.; Fahdiran, R.; Jalil, Z.; Alaydrus, M. Structural, Magnetic and Microwave Absorption Properties of Natural Iron Sand. *J. Phys.: Conf. Ser.* **2021**, *1869*, No. 012182.
(32) Bakhshai, A.; Soika, V.; Susol, M. A.; Takacs, L. Mechanochemical Reactions in the Sn−Zn−S System: Further Studies. *J. Solid State Chem.* **2000**, *153*, 371−380.
(33) Mateti, S.; Mathesh, M.; Liu, Z.; Tao, T.; Ramireddy, T.; Glushenkov, A. M.; Yang, W.; Chen, Y. I. Mechanochemistry: A Force in Disguise and Conditional Effects towards Chemical Reactions. *Chem. Commun.* **2021**, *57*, 1080−1092.
(34) Amir, N.; Tahir, D.; Heryanto, H. Synthesis, Structural and Optical Characteristics of Fe_3O_4/Activated Carbon Photocatalysts to Adsorb Pesticide Waste. *J. Mater. Sci.: Mater. Electron.* **2023**, *34*, No. 445.
(35) Ilyas, S.; Heryanto, H.; Tahir, D. Correlation between Structural and Optical Properties of CuO/Carbon Nanoparticle in Supports the Photocatalytic Performance and Attenuate the Electromagnetic Wave. *J. Environ. Chem. Eng.* **2021**, *9*, No. 104670.
(36) Mohamed, M. A.; Jaafar, J.; Ismail, A. F.; Othman, M. H. D.; Rahman, M. A. *Chapter 1 - Fourier Transform Infrared (FTIR) Spectroscopy*; Hilal, N.; Ismail, A. F.; Matsuura, T.; Oatley-Radcliffe, D. B. T.-M. C., Eds.; Elsevier, 2017; pp 3−29 DOI: 10.1016/B978-0-444-63776-5.00001-2.
(37) Wang, W.; Cao, N.; Dong, J.; Boukherroub, R.; Liu, W.; Li, Y.; Cong, H. Chitosan/Hydroxyapatite Modified Carbon/Carbon Composites: Synthesis, Characterization and in Vitro Biocompatibility Evaluation. *RSC Adv.* **2019**, *9*, 23362−23372.
(38) Szpera, R.; Moseley, D. F. J.; Smith, L. B.; Sterling, A. J.; Gouverneur, V. The Fluorination of C-H Bonds: Developments and Perspectives. *Angew. Chem., Int. Ed.* **2019**, *58*, 14824−14848.

https://doi.org/10.1021/acsomega.3c00423
ACS Omega 2023, 8, 18591−18602

(39) Zenobi, R.; Xu, J.; Yates, J. T.; Persson, B. N. J.; Volokitin, A. I. FTIR Overtone Spectroscopy on Surfaces. The C−O Mode in Chemisorbed Methoxy on Ni(111). *Chem. Phys. Lett.* **1993**, *208*, 414−419.
(40) Blainey, P. C.; Reid, P. J. FTIR Studies of Intermolecular Hydrogen Bonding in Halogenated Ethanols. *Spectrochim. Acta, Part A* **2001**, *57*, 2763−2774.
(41) Shah, M. N.; Patel, N. H.; Shah, D. D.; Mehta, P. K. FTIR: Important Tool to Investigate the Chemical Bond Formation in the Polycrystalline XBaTiO3 − (1-x)BiFeO3. *Mater. Today Proc.* **2021**, *47*, 616−620.
(42) Tahir, D.; Ilyas, S.; Rahmat, R.; Heryanto, H.; Fahri, A. N.; Rahmi, M. H.; Abdullah, B.; Hong, C. C.; Kang, H. J. Enhanced Visible-Light Absorption of Fe2O3 Covered by Activated Carbon for Multifunctional Purposes: Tuning the Structural, Electronic, Optical, and Magnetic Properties. *ACS Omega* **2021**, *6*, 28334−28346.
(43) Khorrami, Gh. H.; Khorsand Zak, A.; Kompany, A.; yousefi, R. Optical and Structural Properties of X-Doped (X=Mn, Mg, and Zn) PZT Nanoparticles by Kramers−Kronig and Size Strain Plot Methods. *Ceram. Int.* **2012**, *38*, 5683−5690.
(44) Tahir, D.; Oh, S. K.; Kang, H. J.; Tougaard, S. Composition Dependence of Dielectric and Optical Properties of Hf-Zr-Silicate Thin Films Grown on Si(100) by Atomic Layer Deposition. *Thin Solid Films* **2016**, *616*, 425−430.
(45) Lahsmin, Y. K.; Heryanto, H.; Ilyas, S.; Fahri, A. N.; Abdullah, B.; Tahir, D. Optical Properties Determined from Infrared Spectroscopy and Structural Properties from Diffraction Spectroscopy of Composites Fe/CNs/PVA for Electromagnetic Wave Absorption. *Opt. Mater.* **2021**, *111*, No. 110639.
(46) Jangong, O. S.; Heryanto, H.; Rahmat, R.; Mutmainna, I.; Gareso, P. L.; Tahir, D. Effect of Sugar Palm Fiber (SPF) to the Structural and Optical Properties of Bioplastics (SPF/Starch/Chitosan/Polypropylene) in Supporting Mechanical Properties and Degradation Performance. *J. Polym. Environ.* **2021**, *29*, 1694−1705.
(47) Nurhasmi, H.; Heryanto, H.; Fahri, A. N.; Ilyas, S.; Ansar, A.; Abdullah, B.; Tahir, D. Study on Optical Phonon Vibration and Gamma Ray Shielding Properties of Composite Geopolymer Fly Ash-Metal. *Radiat. Phys. Chem.* **2021**, *180*, No. 109250.
(48) Hollowood, T. J.; Shore, G. M. The Refractive Index of Curved Spacetime: The Fate of Causality in QED. *Nucl. Phys. B* **2008**, *795*, 138−171.
(49) Tüzemen, E.; Eker, S.; Kavak, H.; Esen, R. Dependence of Film Thickness on the Structural and Optical Properties of ZnO Thin Films. *Appl. Surf. Sci.* **2009**, *255*, 6195−6200.
(50) Johnson, W. R.; Guet, C.; Bertsch, G. F. Optical Properties of Plasmas Based on an Average-Atom Model. *J. Quant. Spectrosc. Radiat. Transf.* **2006**, *99*, 327−340.
(51) Löper, P.; Stuckelberger, M.; Niesen, B.; Werner, J.; Filipič, M.; Moon, S.-J.; Yum, J.-H.; Topič, M.; de Wolf, S.; Ballif, C. Complex Refractive Index Spectra of CH3NH3PbI3 Perovskite Thin Films Determined by Spectroscopic Ellipsometry and Spectrophotometry. *J. Phys. Chem. Lett.* **2015**, *6*, 66−71.
(52) Ghasemifard, M.; Hosseini, S. M.; Khorrami, Gh. H. Synthesis and Structure of PMN−PT Ceramic Nanopowder Free from Pyrochlore Phase. *Ceram. Int.* **2009**, *35*, 2899−2905.
(53) Peng, Z.; Hwang, J.-Y.; Mouris, J. F.; Hutcheon, R. M.; Huang, X. Microwave Penetration Depth in Materials with Non-Zero Magnetic Susceptibility. *ISIJ Int.* **2010**, *50*, 1590−1596.
(54) Shrivastav, A. M.; Satish, L.; Kushmaro, A.; Shvalya, V.; Cvelbar, U.; Abdulhalim, I. Engineering the Penetration Depth of Nearly Guided Wave Surface Plasmon Resonance towards Application in Bacterial Cells Monitoring. *Sens. Actuat., B* **2021**, *345*, No. 130338.
(55) Suryani, S.; Heryanto, H.; Rusdaeni, R.; Fahri, A. N.; Tahir, D. Quantitative Analysis of Diffraction and Infra-Red Spectra of Composite Cement/BaSO4/Fe3O4 for Determining Correlation between Attenuation Coefficient, Structural and Optical Properties. *Ceram. Int.* **2020**, *46*, 18601−18607.
(56) Ardiansyah, A.; Rahmat, R.; Azlan, M.; Heryanto, H.; Tahir, D. Nanocrystal Composites Cement/BaCO3/Fe2O3 for Improved X-Ray Shielding Characteristics: Stability Structural Properties. *J. Mater. Res.* **2022**, *37*, 4114−4123.
(57) Wang, L.; Takeda, S.; Sato, R.; Sakamoto, M.; Teranishi, T.; Tamai, N. Morphology-Dependent Coherent Acoustic Phonon Vibrations and Phonon Beat of Au Nanopolyhedrons. *ACS Omega* **2021**, *6*, 5485−5489.
(58) Baccarelli, P.; Nallo, C.; Paulotto, S.; Jackson, D. In *A Full-Wave Numerical Approach for Modal Analysis of 1-D Periodic Microstrip Structures*; Microwave Theory and Techniques, IEEE Transactions on, 2006; Vol. 54, pp 1350−1362 DOI: 10.1109/TMTT.2006.871353.
(59) Naishadham, K. 4 - Transmission Lines. In *The Electrical Engineering Handbook*; Chen, W.-K., Ed.; Academic Press: Burlington, 2005; pp 525−537 DOI: 10.1016/B978-012170960-0/50040-2.
(60) Yasmeen, S.; Munawar, T.; Asghar, M.; Khan, M. A.; Hussain, A.; Iqbal, F. Synthesis and Photocatalytic Study of Zn0.90Co0.10O and Zn0.90Co0.05M0.05O (M=Ca, Ba, Cr, Pb) Nanocrystals: Structural, Optical and Electrical Investigations. *J. Mater. Res. Technol.* **2020**, *9*, 4076−4096.
(61) Heryanto; Abdullah, B.; Tahir, D.; Mahdalia. Quantitative Analysis of X-Ray Diffraction Spectra for Determine Structural Properties and Deformation Energy of Al, Cu and Si. *J. Phys.: Conf. Ser.* **2019**, *1317*, 12052.
(62) Hosseini, M. A.; Malekie, S.; Keshavarzi, M. Analysis of Radiation Shielding Characteristics of Magnetite/High Density Polyethylene Nanocomposite at Diagnostic Level Using the MCNPX, XCOM, XMuDat and Auto-Zeff Programs. *Moscow Univ. Phys. Bull.* **2021**, *76*, S52−S61.
(63) Alexander, C. L.; Tribollet, B.; Orazem, M. E. Contribution of Surface Distributions to Constant-Phase-Element (CPE) Behavior: 1. Influence of Roughness. *Electrochim. Acta* **2015**, *173*, 416−424.
(64) Szymanik, B.; Frankowski, P. K.; Chady, T.; John Chelliah, C. R. Detection and Inspection of Steel Bars in Reinforced Concrete Structures Using Active Infrared Thermography with Microwave Excitation and Eddy Current Sensors. *Sensors* **2016**, *16*, No. 234.
(65) Lohnes, R. A.; Demirel, T. Strength and Structure of Laterites and Lateritic Soils. *Eng. Geol.* **1973**, *7*, 13−33.
(66) Ma, Y.; Du, X. Effects of CaO Addition on the Iron Recycling from Nickel Slags by Oxidation-Magnetic Separation. *Metals* **2018**, *8*, No. 956.
(67) Ilyas, S.; Heryanto; Abdullah, B.; Tahir, D. X-Ray Diffraction Analysis of Nanocomposite Fe3O4/Activated Carbon by Williamson−Hall and Size-Strain Plot Methods. *Nano-Struct. Nano-Objects* **2019**, *20*, No. 100396.
(68) Heryanto, H.; Tahir, D. High Absorption Electromagnetic Wave Properties of Composite $CoFeO_3$ Synthesized by Simple Mechanical Alloying. *ECS J. Solid State Sci. Technol.* **2021**, *10*, No. 123015.
(69) Williamson, G. K.; Smallman, R. E. III. Dislocation Densities in Some Annealed and Cold-Worked Metals from Measurements on the X-Ray Debye-Scherrer Spectrum. *Philos. Mag.* **1956**, *1*, 34−46.
(70) Tenri Ola, A. T.; Rahmat, R.; Fahri, A. N.; Heryanto, H.; Mutmainna, I.; Sesa, E.; Tahir, D. Synergistic Effect of Chitosan and Activated Carbon (AC) in Suppressing Recombination Charge of Composite Ca2Fe2O5−AC/Chitosan for High Photodegradation of Fipronil Wastewater. *J. Polym. Environ.* **2022**, *30*, 3218−3229.
(71) Rajesh Kumar, B.; Hymavathi, B. X-Ray Peak Profile Analysis of Solid-State Sintered Alumina Doped Zinc Oxide Ceramics by Williamson−Hall and Size-Strain Plot Methods. *J. Asian Ceram. Soc.* **2017**, *5*, 94−103.
(72) Rauf, N.; Ilyas, S.; Heryanto, H.; Rahmat, R.; Fahri, A. N.; Rahmi, M. H.; Tahir, D. The Correlation between Structural and Optical Properties of Zinc Hydroxide Nanoparticle in Supports Photocatalytic Performance. *Opt. Mater.* **2021**, *112*, No. 110780.
(73) Nath, D.; Singh, F.; Das, R. X-Ray Diffraction Analysis by Williamson-Hall, Halder-Wagner and Size-Strain Plot Methods of CdSe Nanoparticles- a Comparative Study. *Mater. Chem. Phys.* **2020**, *239*, No. 122021.

(74) Desai, K. R.; Alone, S. T.; Wadgane, S. R.; Shirsath, S. E.; Batoo, K. M.; Imran, A.; Raslan, E. H.; Hadi, M.; Ijaz, M. F.; Kadam, R. H. X-Ray Diffraction Based Williamson−Hall Analysis and Rietveld Refinement for Strain Mechanism in Mg−Mn Co-Substituted CdFe2O4 Nanoparticles. *Phys. B* **2021**, *614*, No. 413054.
(75) Shirsath, S. E.; Kadam, R. H.; Batoo, K. M.; Wang, D.; Li, S. Co−Al-Substituted Strontium Hexaferrite for Rare Earth Free Permanent Magnet and Microwave Absorber Application. *J. Phys. D: Appl. Phys.* **2021**, *54*, No. 024001.
(76) Hobday, C. L.; Krause, S.; Rogge, S. M. J.; Evans, J. D.; Bunzen, H. Perspectives on the Influence of Crystal Size and Morphology on the Properties of Porous Framework Materials. *Front. Chem.* **2021**, *9*, No. 772059.
(77) Farahani, S. Chapter 5 - RF Propagation, Antennas, and Regulatory Requirements. In *ZigBee Wireless Networks and Transceivers*; Farahani, S., Ed.; Newnes: Burlington, 2008; pp 171−206 DOI: 10.1016/B978-0-7506-8393-7.00005-4.
(78) Li, J.; Liu, P.-F.; Zhang, C.; Shi, X.; Jiang, S.; Chen, W.; Yin, H.; Wang, B.-T. Lattice Vibrational Modes and Phonon Thermal Conductivity of Single-Layer GaGeTe. *J. Materiomics* **2020**, *6*, 723−728.
(79) LATTICE VIBRATIONS: PHONON SCATTERING. In *Electronic and Optoelectronic Properties of Semiconductor Structures*; Singh, J., Ed.; Cambridge University Press: Cambridge, 2003; pp 217−259 DOI: 10.1017/CBO9780511805745.008.
(80) Panigrahi, R.; Srivastava, S. K. Trapping of Microwave Radiation in Hollow Polypyrrole Microsphere through Enhanced Internal Reflection: A Novel Approach. *Sci. Rep.* **2015**, *5*, No. 7638.
(81) Jia, C.; Xia, T.; Ma, Y.; He, N.; Yu, Z.; Lou, Z.; Li, Y. Fe3O4/α-Fe Decorated Porous Carbon-Based Composites with Adjustable Electromagnetic Wave Absorption: Impedance Matching and Loading Rate. *J. Alloys Compd.* **2021**, *858*, No. 157706.
(82) Wang, B.; Wu, Q.; Fu, Y.; Liu, T. A Review on Carbon/Magnetic Metal Composites for Microwave Absorption. *J. Mater. Sci. Technol.* **2021**, *86*, 91−109.
(83) Zhan, Y.; Wang, J.; Zhang, K.; Li, Y.; Meng, Y.; Yan, N.; Wei, W.; Peng, F.; Xia, H. Fabrication of a Flexible Electromagnetic Interference Shielding Fe3O4@reduced Graphene Oxide/Natural Rubber Composite with Segregated Network. *Chem. Eng. J.* **2018**, *344*, 184−193.
(84) Lia, Y.; Zhao, B.; Fan, S.; Liang, L.; Zhou, Y.; Wang, R.; Guo, X.; Fan, B.; Zhang, R. ZnO Amounts-Dependent Electromagnetic Wave Absorption Capabilities of Ni/ZnO Composite Microspheres. *J. Mater. Sci.: Mater. Electron.* **2019**, *30*, 19966−19976.
(85) Liu, J.; Zhao, Z.; Zhang, L. Toward the Application of Electromagnetic Wave Absorption by Two-Dimension Materials. *J. Mater. Sci.: Mater. Electron.* **2021**, *32*, 25562−25576.
(86) Deepthi, K. R.; Ramesh, G. V.; Kodiyath, R.; Murphin Kumar, P. S.; Dakshanamoorthy, A.; Abe, H. Mixed-Valence NaSb3O7 Support toward Improved Electrocatalytic Performance in the Oxygen-Reduction Reaction. *J. Mater. Chem. A* **2017**, *5*, 1667−1671.
(87) Meng, Y. S.; Arroyo-de Dompablo, M. E. First Principles Computational Materials Design for Energy Storage Materials in Lithium Ion Batteries. *Energy Environ. Sci.* **2009**, *2*, 589−609.
(88) Jiang, L.; Yan, H.; Meng, J.; Yin, Z.; Wei, W.; Wang, Y. In *Analysis of Eddy Current Effect and Loss Calculation of Transformer Winding Based on Finite Element Algorithm*, 2017 International Conference on Computer Systems, Electronics and Control (ICCSEC), 2017; pp 405−410 DOI: 10.1109/ICCSEC.2017.8446892.
(89) Udvardi, B.; Kovács, I. J.; Fancsik, T.; Kónya, P.; Bátori, M.; Stercel, F.; Falus, G.; Szalai, Z. Effects of Particle Size on the Attenuated Total Reflection Spectrum of Minerals. *Appl. Spectrosc.* **2017**, *71*, 1157−1168.
(90) Elmahaishi, M. F.; Azis, R. S.; Ismail, I.; Muhammad, F. D. A Review on Electromagnetic Microwave Absorption Properties: Their Materials and Performance. *J. Mater. Res. Technol.* **2022**, *20*, 2188−2220.
(91) Rauf, M.; Khan, A. M.; Ansari, A.; Jilani, M. T.; Shahzeb, T. Skin Depth Verification of the Electromagnetic Waves for Hydrocarbon Detection. *Int. J. Appl. Electromagn. Mech.* **2019**, *60*, 313−326.
(92) Zhai, Y.; Zhu, D.; Zhou, W.; Min, D.; Luo, F. Enhanced Impedance Matching and Microwave Absorption Properties of the MAMs by Using Ball-Milled Flaky Carbonyl Iron-BaFe12O19 as Compound Absorbent. *J. Magn. Magn. Mater.* **2018**, *467*, 82−88.
(93) Izaak, M. P.; Gunanto, Y. E.; Sitompul, H.; Sarwanto, Y.; Ari Adi, W. The Ability of ZnFe2O4 Nanostructure as Electromagnetic Wave Absorber in Frequency Range 2−18 GHz. *Key Eng. Mater.* **2023**, *940*, 31−37.
(94) Yoo, J.-E.; Kang, Y.-M. Electromagnetic Wave Absorbing Properties of Ni-Zn Ferrite Powder−Epoxy Composites in GHz Range. *J. Magn. Magn. Mater.* **2020**, *513*, No. 167075.
(95) Zhou, H.; Jiang, L.; Zhu, S.; Jia, L.; Wu, A.; Zhang, X. Structure Evolution and Electromagnetic-Wave Absorption Performances of Multifunctional FeCoNiMnVx High Entropy Alloys with Harsh-Environment Resistance. *J. Alloys Compd.* **2023**, *946*, No. 169402.
(96) Tahir, D.; Heryanto, H.; Ilyas, S.; Fahri, A. N.; Rahmat, R.; Rahmi, M. H.; Taryana, Y.; Sukaryo, S. G. Excellent Electromagnetic Wave Absorption of Co/Fe<inf>2</Inf>O<inf>3</Inf> Composites by Additional Activated Carbon for Tuning the Optical and the Magnetic Properties. *J. Alloys Compd.* **2021**, *864*. DOI: 10.1016/j.jallcom.2021.158780.
(97) Yousuf, M. A.; Jabeen, S.; Shahi, M. N.; Khan, M. A.; Shakir, I.; Warsi, M. F. Magnetic and Electrical Properties of Yttrium Substituted Manganese Ferrite Nanoparticles Prepared via Micro-Emulsion Route. *Results Phys.* **2020**, *16*, No. 102973.
(98) Nasir, S.; Hussein, M.; Zainal, Z.; Yusof, N. Carbon-Based Nanomaterials/Allotropes: A Glimpse of Their Synthesis, Properties and Some Applications. *Materials* **2018**, *11*, 295.
(99) Pang, J.; Bachmatiuk, A.; Ibrahim, I.; Fu, L.; Placha, D.; Martynkova, G. S.; Trzebicka, B.; Gemming, T.; Eckert, J.; Rümmeli, M. H. CVD Growth of 1D and 2D Sp2 Carbon Nanomaterials. *J. Mater. Sci.* **2016**, *51*, 640−667.

https://doi.org/10.1021/acsomega.3c00423
ACS Omega 2023, 8, 18591−18602